

Lawrence Berkeley National Laboratory

LBL Publications

Title

Elliptic Cylinder Airborne Sampling and Geostatistical Mass Balance Approach for Quantifying Local Greenhouse Gas Emissions

Permalink

<https://escholarship.org/uc/item/75j0z0bk>

Journal

Environmental Science and Technology, 51(17)

ISSN

0013-936X

Authors

Tadić, Jovan M
Michalak, Anna M
Iraci, Laura
et al.

Publication Date



2017-09-05

DOI

10.1021/acs.est.7b03100

Peer reviewed

Elliptic Cylinder Airborne Sampling and Geostatistical Mass Balance Approach for Quantifying Local Greenhouse Gas Emissions

[Jovan M. Tadić](#)[†] , [Anna M. Michalak](#)[†], [Laura Iraci](#)[‡], [Velibor Ilić](#)[§] , [Sébastien C. Biraud](#)^{||}, [Daniel R. Feldman](#)^{||}, [Thaopaul Bui](#)[‡], [Matthew S. Johnson](#)[‡], [Max Loewenstein](#)[‡], [Seongeun Jeong](#)[⊥], [Marc L. Fischer](#)[⊥], [Emma L. Yates](#)[‡], and [Ju-Mee Ryoo](#)[‡]

[†] Department of Global Ecology, Carnegie Institution for Science, Stanford, California 94305, United States

[‡] Earth Science Division, NASA Ames Research Center, Moffett Field, California, United States

[§] RT-RK Institute for Computer Based Systems, 21000 Novi Sad, Serbia

^{||} Earth and Environmental Sciences Area, Lawrence Berkeley National Lab, Berkeley, California 94720, United States

[⊥] Energy Technologies Area, Lawrence Berkeley National Lab, Berkeley, California 94720, United States

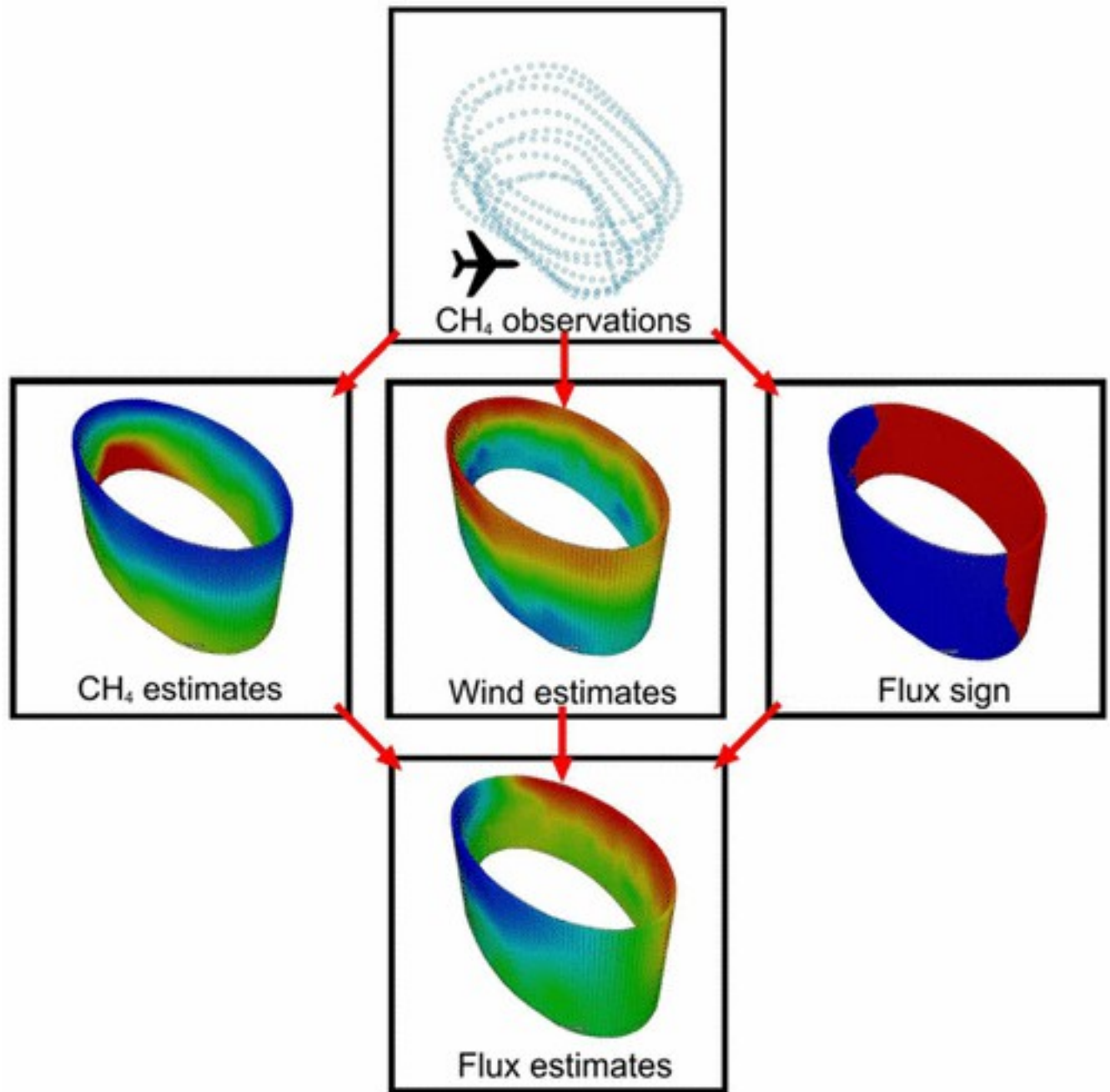
DOI: 10.1021/acs.est.7b03100

Publication Date (Web): July 20, 2017

*E-mail: jotadic@lycos.com.

•

Abstract



In this study, we explore observational, experimental, methodological, and practical aspects of the flux quantification of greenhouse gases from local point sources by using in situ airborne observations, and suggest a series of conceptual changes to improve flux estimates. We address the major sources of uncertainty reported in previous studies by modifying (1) the shape of the typical flight path, (2) the modeling of covariance and anisotropy, and (3) the type of interpolation tools used. We show that a cylindrical flight profile offers considerable advantages compared to traditional profiles collected as curtains, although this new approach brings with it the need for a

more comprehensive subsequent analysis. The proposed flight pattern design does not require prior knowledge of wind direction and allows for the derivation of an ad hoc empirical correction factor to partially alleviate errors resulting from interpolation and measurement inaccuracies. The modified approach is applied to a use-case for quantifying CH₄ emission from an oil field south of San Ardo, CA, and compared to a bottom-up CH₄ emission estimate.

1 Introduction

Atmospheric measurements at local scales can be used to provide a top-down constraint on emissions as well as to validate and improve bottom-up emission inventories. Local scale measurements can target various local sources, ranging from the anthropogenic (urban centers, industrial activities, agriculture, traffic, landfills) to the natural (volcanoes, wild fires, marshlands). The lack of a standardized verification protocol for measuring GHG fluxes from point sources has led to uncertainty in quantifying, and by extension, mitigating these point sources. This situation is particularly problematic because urban populations are expected to double by 2050⁽¹⁾ and will significantly influence GHG emissions, but mechanisms to characterize these emissions are lacking. Quantitative measurement, reporting, and verification (MRV) will be critical to any international climate treaty, as emphasized by a 2010 National Research Council (NRC) report,⁽²⁾ and by the Intergovernmental Panel on Climate Change.⁽³⁾ Verification based on direct observations of atmospheric GHG concentrations could provide estimates of emission reductions.⁽⁴⁾

To fill this need, the quantification of GHG emissions at high spatial resolutions has become an area of active research. The highly heterogeneous nature of anthropogenic emissions does not lend itself well to the application of inverse modeling tools developed primarily for regional/continental scale estimation of biospheric fluxes.⁽⁵⁾ Several recent studies have examined the feasibility of constraining greenhouse gas emissions at local scales using ground-based,^(4, 6) airborne,⁽⁷⁻¹¹⁾ and space-based⁽¹²⁾ observations. Airborne observations, in particular, offer an opportunity to capture GHG concentrations in the air entering and exiting a focus area. Flux studies using airborne measurements have also been conducted at local scales from sources such as forest fires,⁽¹³⁾ volcanoes,⁽¹⁴⁾ leaks from natural gas and oil operations^(15, 16) and related accidents,⁽¹⁵⁾ emissions from dairy farms,^(17, 18) and landfills.⁽¹⁸⁾

Early applications of airborne observations for quantifying local and urban emissions have exposed the high uncertainties associated with baseline mass balance approaches at spatial scales of 10s to

100s of km. For example, a study in Indianapolis⁽⁷⁾ reported uncertainties of 80% (19.2 ± 15.4 $\mu\text{mol}/\text{m}^2\text{s}$) for CO_2 emissions, and 71% (0.14 ± 0.10 $\mu\text{mol}/\text{m}^2\text{s}$) ($\pm 1\sigma$) for CH_4 . The flux quantification method used in that study relied on airborne observations along a single downwind “curtain” in combination with a kriging scheme, presuming direction-independent (constant) variability and mass balance. In more recent studies, uncertainty estimates were reduced to $\sim 43\%$ ($\pm 1\sigma$) for CH_4 emissions from Indianapolis,⁽¹⁹⁾ $\sim 30\%$ ($\pm 1\sigma$) for CH_4 and SO_2 emissions from Alberta oil sands operations,⁽¹¹⁾ and $\sim 29\%$ (95% confidence interval (CI)) for CH_4 emissions from the Barnett Shale basin.⁽²⁰⁾ The uncertainty reduction is achieved through more sophisticated quantification protocols: (a) introduction of a second, up-wind curtain^(8, 10, 11) that captures both the upwind and downwind concentration profiles, and (b) the reduction of measurement time by using a second aircraft flying dense horizontal transects to reduce interpolation errors.

More recent work using aircraft to measure GHG emissions at small (~ 1 km) spatial scales has claimed that methane emissions from an individual facility can be measured to better than 20% by combining in situ measurements of winds and GHG concentration measurements using mass-flux integration over controlled flight patterns covering the vertical extent of plumes downwind of individual facilities.⁽¹⁵⁾

The factors contributing to uncertainties in the quantification of fluxes from localized or point sources using airborne measurements are listed and analyzed in Cambaliza et al. (2014).⁽⁹⁾ The factors for these large uncertainties generally fall into four categories: (1) observational, related to the ability of the flight plan or sampling scheme to capture urban emissions and background concentrations, the requirement for many horizontal transects to get reasonable coverage, and the necessity to know wind direction in advance for flight path planning; (2) experimental, related to the availability of reliable, accurate, and high frequency airborne sensors for all measured quantities, including wind speeds and GHG concentrations; (3) practical, involving air traffic control problems encountered around urban centers; and (4) methodological, pertaining to the availability of postprocessing/modeling tools that accurately and precisely translate the observed spatiotemporal GHG concentration patterns into GHG fluxes and their associated uncertainties and the failure to exploit existing and observed spatial concentration trends (especially characterizing the concentration field below the aircraft profile).

In this study, we focus on the major observational, experimental and methodological factors limiting the precision of GHG flux estimation at local/facility scales. We explore if and how modifying sampling protocols might be expected to reduce uncertainty for these facility-scale flux estimates and perhaps larger spatial scales if large-scale entrainment and convection can be estimated. Our

suggested modifications include (1) changes in flight patterns, (2) interpolation techniques and associated modeling of spatial variability, (3) reduction in sampling time, and (4) a revised the approach to mass balance. For the first modification, we use a flight pattern design that maximizes capture of inflow and outflow, and eliminates the need for prior knowledge of the predominant wind direction ([Section 2.1](#)). For the second modification, we develop a geostatistical approach that accounts for anisotropy (zonal or directionally dependent variability) and variable spatial means of atmospheric GHGs ([Section 2.2.2](#), [2.2.3](#), and [Supporting Information \(SI\)](#)). For the third modification, we use winds measured by the aircraft simultaneous to the GHG concentration measurements. For the final modification, we use a mass balance approach not only to quantify the flux of the atmospheric constituent of interest, but also to derive an empirical correction factor to account for dynamic effects of mass convergence within the domain of field measurements. ([Section 2.2.4](#)). These tools and approaches apply broadly to a range of local/urban domains and choices of single or multiple airborne platforms, including aircraft and unmanned aerial systems (UAS) and can reduce uncertainty in mass balance characterization across spatial domains of 10s of km.

2 Materials and Methods

2.1 Aircraft and Instruments

We developed and tested the cylindrical sampling and geostatistical mass balance approach by collecting and analyzing data from a flight covering a 4×9 km area surrounding an oil field about 8 km south of San Ardo, CA ($35^{\circ}57'$ N, $120^{\circ}52'$ W), on 10/01/2015. This area includes the eighth largest oil-producing field in California with 7.8 million barrels of oil, and ~ 1 million Mcf of natural gas produced in 2015.[\(21\)](#) The flight took place at around 20:30 UTC (local time 12:30 PM), a time when the planetary boundary layer (PBL) has not yet reached its peak. Due to quick sampling (10–15 min), it is reasonable to assume that the PBL top remains at a stable height during the aircraft sampling period.

Measurements were collected using an aircraft (Alpha Jet) based at the National Aeronautics and Space Administration (NASA) Ames Research Center, equipped with a Picarro 2301-m cavity ring-down instrument for CO_2 , CH_4 and H_2O measurements, GPS and inertial navigation systems that provide latitude, longitude and altitude, and a Meteorological Measurement System (MMS), which measures both dynamic and static state variables. MMS, a NASA Ames-developed airborne instrument package, provides calibrated, science-quality, in situ measurements of static pressure, static temperature, wind in three dimensions, GPS positions, velocities, accelerations, pitch, roll,

yaw, heading, angle of attack, angle of sideslip, dynamic total pressure, and total temperature. The primary products of MMS are barometric pressure (precision of 0.1 hPa with an accuracy of ± 0.3 hPa), air temperature (0.1 K, ± 0.3 K), horizontal wind (0.1 ms^{-1} , ± 1 ms^{-1}), and vertical wind (0.1 ms^{-1} , ± 0.3 ms^{-1}) (<https://airbornescience.nasa.gov/instrument/MMS>). Other derived parameters are potential temperature, true air speed, turbulence dissipation rate, and Reynolds number. This instrument has been installed in several NASA aircraft in addition to the Alpha Jet, including the ER-2, the DC-8, and the Global Hawk unmanned aircraft, the WB-57F, and is flexible in terms of flight pattern (i.e., not limited to straight or level flights only). Further details of the aircraft and instruments can be found in previous publications. [\(22-24\)](#)

2.2 Theory

2.2.1 Optimization of the Projection Grid

Cylinder-shaped profiles offer a substantial advantage over the “curtain” type flight profile, because they can necessarily adapt to any wind direction. In other approaches, the wind direction needs to be determined either ahead of the flight or at the start of the sampling phase, whereas in this approach this constraint is relaxed. However, this approach requires a more sophisticated subsequent analysis for calculating fluxes ([Section 2.2.4](#)).

Before the fitting, interpolations and flux calculation, all spatially referenced data are converted to a Universal Transverse Mercator (UTM) (Euclidean) coordinate system, so that distances and angles can be computed using Euclidean geometry over short distances. [\(25\)](#) The GPS instrument records raw data in latitude/longitude/altitude format based on WGS84 spheroid earth model. [\(26\)](#) The additional uncertainty in the position of the aircraft introduced by the spatial distortions in conversion to UTM system is <1 mm and is therefore negligible compared to the 3–4 m horizontal uncertainty in position reported by the GPS instrument.

An optimal 3D elliptical grid is fitted to the flight trajectory following a three-step approach. First, we fit the optimal ellipse into a vertically projected set of coordinates representing the flight trajectory. Next we place an arbitrary number of equidistant points (300 in this case) along the perimeter of the ellipse optimized in the first step. In general, the optimal number of points depends on the observed spatial variability of all relevant variables. The potential dependence of the results on details of optimal grid construction and projection can be considered heuristically. The third step is the extension of the discretized elliptical profile obtained in the second step and involves matching the ceiling of the flight trajectory (every 50 m up to ~ 2550 m).

Only nodes of the grid that reside above the ground level are contained in the final projection grid, and customized software built on Google Maps elevation data

(<https://developers.google.com/maps/documentation/elevation/intro>) is used to eliminate underground points on the grid. The result is an optimal 3D projection grid used for interpolation, projection, and flux calculation.

2.2.2 Original Product-Sum Model and Proposed Modifications

In this study we develop an alternative kriging approach for modeling an anisotropic environment, using a product-sum covariance model.[\(27-29\)](#)

This product-sum was initially developed for different purposes - to model spatiotemporal covariance structures in which a common unit of the distance between points does not exist because of the different natures of spatial and temporal axes. We observe that there is an analogy between problems of modeling spatiotemporal covariance and covariance in anisotropic conditions. In modeling spatiotemporal variability, it is necessary to deal with two qualitatively different spatiotemporal subspaces. Formally, the variability in these spatiotemporal subspaces could require different theoretical variogram models, and requires different units of distance.[\(30\)](#) In anisotropy, we face an analogous situation, with potentially different types of variability in different directions. Therefore, the product-sum model is applicable to anisotropic conditions, and, as we show in this study, equivalent to the classical model of zonal anisotropy in the case where horizontal and vertical directions represent principal anisotropic axes (i.e., when anisotropy splits the space into two subspaces). We show that there is a partial mathematical equivalency between these two models, in the sense that every admissible set of sill parameters in the classical model (three sill parameters, seven parameters in total) can be expressed as an admissible set of sill parameters (three sill parameters, six parameters in total) in the product-sum model. The sill is the expected value of the semivariance between two observations as the lag distance tends to infinity.[\(30\)](#)

There is one important area for improvement in the manner that the product-sum model has been applied in the past. The original procedure[\(27\)](#) assumed separate modeling of the spatial and temporal covariance (variograms) and their later unification into a spatiotemporal model in the final step. In our study, this is equivalent to separating modeling the vertical and horizontal covariance, if we assume temporal stationarity of the wind and concentration fields (this assumption could be problematic in that there is a risk of using the same air parcel as it advects to a different location, which, when combined with the potential that the field is actually nonstationary in composition, could lead to artifacts in the analysis). The procedure requires observations approximately in the same horizontal location at multiple different altitudes. However, aircraft trajectories are often not perfectly horizontally collocated at different altitudes. As a result, we would need to define a tolerance in order to apply the original approach, which is also a part of the genuine modeling approach suggested in

De Iaco et al., 2001. (27) To avoid defining a tolerance, in this study we cater to specific properties of aircraft trajectories and alter the original procedure by estimating all covariance parameters simultaneously.

We broadly define the covariance as follows: $C_{h,v}(h_h, h_v) = \text{COV}(Z(l_h + h_h, l_v + h_v), Z(l_h, l_v))$ (1)

The equation shows that covariance ($C_{h,v}$) between two points (Z) depends on their distance in horizontal direction (h_h) and distance in vertical direction (h_v). l_h and l_v denote arbitrary horizontal and vertical coordinate within the domain. The product-sum covariance model is given as $C_{h,v}(h_h, h_v) = k_1 C_h(h_h) C_v(h_v) + k_2 C_h(h_h) + k_3 C_v(h_v)$ (2) where C_v and C_h are valid vertical and horizontal covariance models, respectively. (27, 29) This model corresponds to the horizontal-vertical variogram: $\gamma_{h,v}(h_h, h_v) = \gamma_{h,v}(h_h, 0) + \gamma_{h,v}(0, h_v) - k \gamma_{h,v}(h_h, 0) \gamma_{h,v}(0, h_v)$ (3) where $\gamma_{h,v}(h_h, 0)$ and $\gamma_{h,v}(0, h_v)$ are spatiotemporal variograms for $h_v = 0$ and $h_h = 0$, respectively (see Figure 1 (red lines)).

In the original procedure, separately estimated horizontal (“spatial”) and vertical (“temporal”) variogram components are subsequently combined into a horizontal-vertical variogram model, equivalent to spatiotemporal variogram in the genuine embodiment of the approach.

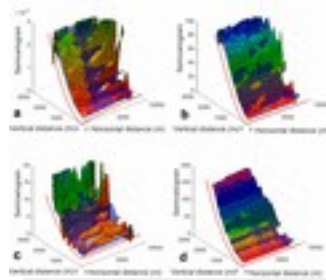


Figure 1. Horizontal-vertical 2D experimental (rainbow) and theoretical variograms (transparent blue) based on the product-sum covariance (variogram) model for (a) CH₄ (ppm), (b) U (E-W) (m/s), (c) V (N-S) (m/s), and (d) temperature (K). Red lines starting from the origin show isolated vertical, $\gamma_{h,v}(0, h_v)$, and horizontal, $\gamma_{h,v}(h_h, 0)$, variability represented using Gaussian (vertical) and exponential (horizontal) variogram model, respectively. Theoretical variograms were fitted directly using raw spatiotemporal variograms (eq 3), and experimental variograms are shown only for demonstrative purposes.

$$k = \frac{k_h C_h(0) + k_v C_v(0) - C_{h,v}(0, 0)}{k_h C_h(0) k_v C_v(0)} \quad (4)$$

Parameter k is estimated from the data:

where $k_h C_h(0)$

and $k_v C_v(0)$ are horizontal and vertical sills (variances) obtained in modeling of separate horizontal

and vertical variograms. The only condition k has to fulfill in order to create an admissible covariance

model is $0 < k \leq \frac{1}{\max\{\text{sill}(\gamma_{h,v}(h_h, 0)); \text{sill}(\gamma_{h,v}(0, h_v))\}}$ (5)

Due to the specifics of airborne data, we estimated both the covariance parameters and parameter k simultaneously. This approach accounts for constraints that ensure that the model is positive-definite.[\(27\)](#) This simultaneous approach makes the model more applicable to scattered data and data with variable spatial coverage, as is often the case with airborne observations. The choice of Gaussian and exponential variogram model for all state variables was made based upon visual inspection of the variograms (alternatively, the choice could have been done purely based on the quality of fit). The forms of these variograms are as follows:

$$\gamma_v(h_v)(\text{Gaussian}) = \begin{cases} 0, & \text{for } h_v = 0 \\ \sigma_v^2 \left(1 - \exp\left(-\frac{h_v^2}{l_v^2}\right) \right) + \sigma_{\text{nug}}^2, & \text{for } h_v > 0 \end{cases} \quad (6)$$

$$\gamma_h(h_h)(\text{exponential}) = \begin{cases} 0, & \text{for } h_h = 0 \\ \sigma_h^2 \left(1 - \exp\left(-\frac{h_h}{l_h}\right) \right) + \sigma_{\text{nug}}^2, & \text{for } h_h > 0 \end{cases} \quad (7)$$

where σ_v^2 and σ_h^2 are the

variances, l_v and l_h correlation length parameters of the quantity being mapped, and σ_{nug}^2 is the nugget variance, typically representative of measurement errors or microscale variability. The term nugget arises from the field of variography and is defined as a discontinuity of the covariance or variogram at the origin.[\(30\)](#)

Unlike the original procedure in De Iaco et al. (2001),[\(27\)](#) we modeled the variogram using only three steps. First, we calculated a raw horizontal-vertical variogram:

$$\gamma(h_h, h_v) = \frac{1}{2} [y(x_i) - y(x_j)]^2 \quad (8)$$

where γ is the raw horizontal-vertical variogram value for a given

pair of observations $y(x_i)$ and $y(x_j)$, and h_h and h_v are the horizontal and vertical distances between the measurement locations (x_i and x_j), respectively.

Subsequently, the theoretical variogram defined in [eq 3](#) was fitted to the raw variogram using nonlinear least-squares. Finally, we calculated the horizontal-vertical covariance using the following equation:
 $C_{h,v}(h_h, h_v) = C_{h,v}(0, 0) - \gamma_{h,v}(h_h, h_v)$ [\(9\)](#)

Classical versus Novel Approach

As stated earlier, in the classical approach to modeling zonal anisotropy, a nested variogram structure is required for every direction in which zonal anisotropy is identified. Applied to a specific case of zonal anisotropy (often found in PBL), where principal anisotropic subspaces represent horizontal and vertical directions, the classical approach to modeling zonal anisotropy is given by

equation:[\(30\)](#)
$$\gamma(h) = \gamma_1(\sqrt{h_x^2 + h_y^2 + h_z^2}) + \gamma_2(\sqrt{h_x^2 + h_y^2}) + \gamma_3(h_z)$$

(10) Where h_x and h_y represent distances in orthogonal horizontal directions, and h_z represents vertical distance. Nested variogram structures required for separate modeling of the horizontal (y_2) and vertical (y_3) directions increase the number of estimated parameters to seven, if modeling is based upon most common theoretical variogram (covariance) models, for example exponential or Gaussian (three sills, three range parameters and a nugget). If we denote with “S” the sills corresponding to y_1 , y_2 , and y_3 in classical approach, from [eq 10](#) it follows that the vertical sill is S_1+S_3 (corresponding to y_1 and y_3 , after setting h_x and h_y to zero), the horizontal sill is S_1+S_2 (corresponding to y_1 and y_2 , after setting h_z to zero), whereas in all other directions the sill is given as $S_1+S_2+S_3$. Fitting such a model to the experimental data, especially in the case of noisy and/or sparse observations, is nontrivial. As reported by De Iaco et al. (2001),[\(27\)](#) fitting the model to the data was identified as one of two major problems when modeling spatiotemporal variograms. In this section we show that in this novel approach, fewer parameters have to be estimated (6 vs 7). This can be done either simultaneously or sequentially, where the latter approach is used in the original implementation of the method described in De Iaco et al. (2001).[\(27\)](#) From [eq 5](#) it follows that the alternative approach is guaranteed to yield positive definite covariance functions if parameter k (“global sill”) in the product-sum model is between the sum of sills and the larger separate sill. The comparison between [eqs 3](#) and [10](#) shows that partial sills ($k_h C_h(0)$ and $k_v C_v(0)$) in the product-sum model correspond to sills S_1 , S_2 , and S_3 in the classical approach in a straightforward way. $k_h C_h(0) = S_1 + S_2$ (horizontal sill) [\(11\)](#) $k_v C_v(0) = S_1 + S_3$ (vertical sill) [\(12\)](#) $k = S_1 + S_2 + S_3$ (global sill) [\(13\)](#)

Thus, the requirement for the positive definiteness in the product-sum model ([eq 5](#)) expressed as sill values in the classical approach can be rewritten as $\max(S_1 + S_3, S_1 + S_2) < S_1 + S_2 + S_3 < 2S_1 + S_2 + S_3$ [\(14\)](#) which is true for any positive set of values for S_1 , S_2 , and S_3 . It follows that every possible combination of S_1 , S_2 , and S_3 in the classical approach is guaranteed to fulfill the admissibility requirements of the product-sum model, that is, three sills in the product-sum model can be parametrized in a way that corresponds to partial sill values in the classical modeling approach. Thus, these two approaches are equivalent in terms of modeling variances along principal axes of anisotropy, however, the product-sum model is more practical in that its parameters are more easily estimated with either a simultaneous or sequential approach.

2.2.3 Kriging Using Covariance Structure Based on Product-Sum Model

Most common approaches to atmospheric interpolation use various forms of kriging. [\(7, 9, 11, 20, 31\)](#) Kriging is a geostatistical interpolation method in which the estimated value is expressed as a linear combination of known/measured values. The approach is based on first modeling the spatial

covariance structure of the data, usually through a process known as variography or variogram analysis.(30) Estimation of interpolation uncertainties is also obtained as part of kriging. In the majority of atmospheric studies, a relatively simple kriging method based on the assumption of isotropic variogram (covariance) kernels is used, which cannot account for the anisotropic atmospheric structure. Chilès and Delfiner (2012)(30) describe details of the mathematical foundations of kriging.

In addition to the problem of isotropy/anisotropy, the presumption of a constant mean within the examined spatial domain should be objectively evaluated. In Tadić et al. (2015a),(31) a universal kriging(30, 32, 33) method was substituted for ordinary kriging, because the assumption of a constant mean in the vertical direction was found not to be valid. That study highlighted the need to assess trends in the observations, and to implement a statistical model consistent with observed variability.

The variance-ratio test(34) is used here to assess whether the introduction of a more complicated model of the mean is justified. Although a trend with more auxiliary variables will always be able to represent more of the inferred variability relative to a simpler model, including auxiliary variables with only a spurious correlation to mixing ratio can bias the model and yield unreasonable estimates in poorly constrained areas.(35) In the variance-ratio test, the weighted sum of squares (WSS) of the orthonormal residuals is defined for an initial (\mathbf{X}_0 (constant mean), $n \times p$) and an augmented (\mathbf{X}_1 (height and height square used as covariates), $n \times (p + q)$) model of the trend (where \mathbf{X}_0 is a subset of \mathbf{X}_1) as $WSS_0 = \mathbf{z}^T (\mathbf{Q}^{-1} - \mathbf{Q}^{-1} \mathbf{X}_0 (\mathbf{X}_0^T \mathbf{Q}^{-1} \mathbf{X}_0)^{-1} \mathbf{X}_0^T \mathbf{Q}^{-1}) \mathbf{z}$ (15) $WSS_1 = \mathbf{z}^T (\mathbf{Q}^{-1} - \mathbf{Q}^{-1} \mathbf{X}_1 (\mathbf{X}_1^T \mathbf{Q}^{-1} \mathbf{X}_1)^{-1} \mathbf{X}_1^T \mathbf{Q}^{-1}) \mathbf{z}$ (16) where \mathbf{Q} is the (generalized) covariance matrix of the data, \mathbf{z} is vector of observations, \mathbf{X}_0 corresponds to constant mean presumption, and \mathbf{X}_1 corresponds to a model with two explanatory variables, height and height squared. The derivation of the Variance Ratio Test can be found in [eqs 1-11](#) in the original paper.

The significance of the improvement in model fit is evaluated using the empirical probability

$$v = \frac{\frac{WSS_0 - WSS_1}{p}}{\frac{WSS_1}{(n - p - q)}}$$

distribution of the normalized relative difference between WSS_0 and WSS_1 , (35)

(17) and the significance level is quantified using an F -distribution with q and $n-p-q$ degrees of freedom (where n represents the number of available measurements, p the number of components in \mathbf{X}_0 , and q the number of additional components in \mathbf{X}_1 relative to \mathbf{X}_0 , p and q equal 1 and 2, respectively). In this study the variance-ratio test shows that the inclusion of explanatory variables is

not justified (see [Section 3.2](#)), so we use ordinary kriging based on an anisotropic kernel.

Nevertheless, in a generalized approach, the universal kriging may be a viable option.

2.2.4 Flux Calculation Framework

In other studies, the mass flow (mol s^{-1}) through the plane perpendicular to the wind vector, downwind of the point source, is usually obtained through integration of the products of the concentration (mol m^{-3}) enhancement above the background concentration $[C]_b$ and the component of the wind vector perpendicular to the plane (U_{\perp}): [\(9, 36\)](#)

$$F = \int_{z(\text{sfc})}^{z_i} \int_{-x}^x ([C] - [C]_b) \times U_{\perp} dx dz$$

(18) where z_i is the depth of the convective boundary layer, $z(\text{sfc})$ is the ground level, and $\pm x$ are the horizontal limits of the plume width from the center point (for details on how relevant variables were estimated in earlier studies, see Cambaliza et al. (2014) [\(9\)](#)). The integration gives flux in mol s^{-1} .

In practice, even under the stationarity assumption, applying [eq 18](#) can still be problematic. First, a basic prerequisite for calculating the concentration enhancement is the knowledge of the background concentration of the compound of interest. Second, the optimal position of the standard measurement curtain(s) is perpendicular to the wind vector, which assumes knowledge of the field prior to the flight, or the ability to diagnose and adjust the flight plan upon arrival at the sampling location.

The cylindrical flight profile proposed in this study, in conjunction with a new way to model the covariance structure, avoids both of these problems. Specifically, the cylindrical flight (and grid) profile relaxes the requirement of prior knowledge of the wind directions, as some parts of the grid are guaranteed to be nearly perpendicular to the wind vector. Second, instead of integrating the wind (\perp) \times concentration to the top of the PBL and width of the plume, the product is integrated over the

$$F = \int_0^P C \times U_{\perp} dP \cong \sum_{i=1}^N p_i C_i U_{\perp i}$$

entire grid. After these modifications, [eq 18](#) becomes

(19) where C is observed (interpolated) concentration, N is number of nodes on the grid, P is its surface area, and p_i is the area each node represents, given as P/N . The projection of the wind vector on the direction normal to the grid at each node is done in UTM (Euclidean) space after transformation is done ([Section 2.2.1](#)). In this approach, there is no need to isolate the plume from the background concentration.

To calculate the fluxes using [eq 19](#), the unit surface vectors are first isolated at every node on the grid, and then the vector dot product between the total wind vector and unit surface vector is calculated. It gives the normal wind vector component at every node.

Mixing ratios of all constituents of interest, in this case CO_2 , CH_4 , and temperature, pressure and wind vector components are interpolated to the grid using an ordinary kriging scheme, based on the

results of variance-ratio test(34) (see [Section 3.2](#) for details on the method selection), coupled with product-sum covariance models presented in [Section 2.2.2](#). Mixing ratios at each node are subsequently converted to absolute concentrations. The surface area for each node is calculated by dividing the entire grid surface by the number of nodes. The flux was then calculated using [eq 19](#). The new approach offers one additional way of controlling wind interpolation and measurement errors compared to “curtain” approaches. Namely, the flux of the background air through the entire grid must be zero, as there is no accumulation or depletion of the air mass within the grid under the presumption that pressure and temperature are not changing significantly during the observation period, and that there is no ventilation through the top of the grid. This condition is equivalent to

$$F_{\text{air}} = \oint_p^0 C_{\text{air}} \times U_{\perp} dP = 0 \quad (20)$$

The air density at every node is calculated using the ideal gas law: $C = P_r/RT$

(21) where P_r and T are pressure and temperature at the node, respectively, and R is universal gas constant ($\sim 8.31 \text{ Jmol}^{-1}\text{K}^{-1}$). [eq 20](#) indirectly provides an empirical correction factor (see below), which can be used to correct flux estimates for the compound of interest due to accumulated wind measurement and interpolation errors, building off the point-wise kriging error analysis and their cumulative effect on flux calculations as discussed in Cambaliza et al. (2014). (9) After the calculation of air inflow and outflow from the grid, the imbalance in these quantities indicates the degree to which wind measurements and interpolations are inaccurate. According to Mays et al. (2009), (7) wind measurements represent the highest uncertainty factor in flux quantifications from point sources. The maximum likelihood estimate of true air flux through upwind and downwind portions of the cylindrical grid is given as the arithmetic mean of the entire inflow and outflow air fluxes,

$\hat{F}_{\text{air}} = \frac{1}{2}(F_{\text{air}}^{\text{inflow}} + F_{\text{air}}^{\text{outflow}})$, through up- and downwind portions of the grid. Thus, the ratio between measured and mean air flux serves as an empirical correction factor that can be applied to inflow and outflow flux of any constituent of the air under the assumption that errors in wind measurements and interpolations equally affect background air and its constituents, or, in other words, that the ratio between F_{air} and measured inflow and outflow of the air can be applied as a correction factor to total inflow and outflow of the compound of interest. One additional weak assumption is required here, namely that the correction factor is equally applicable to all nodes, or that the error distributions are flat, because the correction factor is calculated for the entire inflow and outflow portion of grid surface, but applies locally to every node.

The derivation of the empirical correction factor represents the third and last significant contribution of this study to the development of urban outflow sampling protocols. It is made possible by

switching from planar “curtain”-shaped flight profiles to cylindrical flight profiles, and alleviates the errors stemming from inaccurate wind measurements and interpolations as one of the most important sources of flux estimation uncertainty. The physics of the model assume an impermeable lid of the cylinder, and applicability of the method directly depends on the validity of this presumption. This presumption is appropriate when the fraction of source emissions leaving through the “lid” of the cylinder is small. It can be evaluated by analyzing the shape and intensity of the plume passing through the grid. Since it is reasonable to expect that emissions create a continuous plume, especially if there is only one source, the presence of a plume that is contained within the grid and well below the upper edge of the cylinder justifies the presumption that there is little or no uplift that would affect the emission calculation.

3 Results and Discussion

3.1 Variogram Analysis

[Figure 1](#) shows experimental and theoretical variograms based on the product-sum covariance (variogram) model for CO₂, CH₄, H₂O, temperature, and two wind components (U(E-W) and V(N-S)). After close visual examination of the experimental variograms, we chose Gaussian and exponential theoretical variogram models to represent separate vertical and horizontal components within the product-sum model. The resulting variogram confirmed a strong case of zonal anisotropy (different sills and ranges in horizontal and vertical directions). This reconfirmed that proper modeling of the covariance within the PBL must account for a possible presence of zonal anisotropy due to stratification. [Figure 1](#) shows clearly that omnidirectional theoretical models could hardly fit the observed experimental variogram shape(s), due to a significant difference in variogram (covariance) parameters along horizontal and vertical directions. Variogram analysis yielded optimized product-sum covariance models for all variables, which were subsequently used in an ordinary kriging interpolation scheme.

3.2 Kriging the Measured Data

Before we selected the optimal kriging method, we ran the variance-ratio test([34](#)) to check if the more complex model of the mean (using height and height-squared as covariates) would be needed in this particular case ([Section 2.2.3](#)). Results showed that vertical gradients were not sufficient to justify the implementation of a more complex model of the mean for parameters measured during these two flights. Thus, the subsequent analysis used ordinary kriging based on the anisotropic

kernel ([Section 2.2.2](#)) on all variables (CH₄ mixing ratio, pressure, temperature, and horizontal wind speed components).

[Figure 2](#) shows the results of kriging CH₄, and U and V wind vector components to the projection grid. The relative enrichment in CH₄ concentrations on the downwind sections of the grid is apparent, which qualitatively confirms the emission activity at the site.

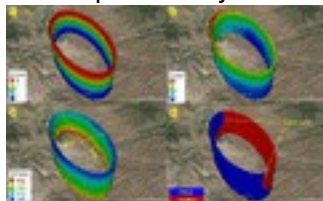


Figure 2. (a) Absolute values of U (m/s) and (b) V (m/s) wind vector components on the projection grid, (c) ordinary kriged CH₄ (ppm), (d) wind direction. (Background images: Google, Landsat/Copernicus).

Elliptical grid shape allows convenient visual representations of the wind field. The apparent feature in [Figure 2d](#) is the appearance of the perfect Ekman spiral. [\(37\)](#) The Ekman spiral, a consequence of the Coriolis Effect, is a structure of currents or winds that occurs near a horizontal boundary (here the ground surface) in which the flow direction rotates as one moves away from the boundary. [\(37\)](#) Our study provides a measure of the consistency of wind estimates through integration of the flux (mass flow) of the air through upwind and downwind portions of the grid. In an ideal case, the ratio should be close to unity, such that any deviation from unity can be solely attributed to the emission from the source. In a real-world case, the deviation from unity would also result from inaccuracies in the wind estimates, interpolations, problems with the physics of the model (e.g., basic presumptions, like the absence of the vertical mass transfer), and variability in the emission activity of the source.

The ratio between outflow and inflow (computed as $(\sum_{i=1}^N P_i C_{i,air} U_{Li})_{inflow} / (\sum_{i=1}^N P_i C_{i,air} U_{Li})_{outflow}$) was found to be 0.989. The imbalance cannot be explained purely by the emission activity of the source, as, for example, the effects of 10% change in relative humidity would lead to 2 g/kg in concentration units (at 760 Torr and 25 °C), whereas the observed imbalance of 1% of air translates into ~12 g/kg, in concentration units.

We also calculated the fraction of the overall air flux through the grid that passes below the lowest measured point (below flight trajectory, approximately at 350 m amsl), because expected interpolation uncertainty is highest in that area. We found that only 1.5% of the overall flux of air passing through the grid actually passes below the flight trajectory.

3.3 Flux Calculation and Uncertainty Quantification

The flux calculation method presented in Section 2.2.6, together with the ordinary kriging approach, was applied to quantify CH₄ emission from the target site. The approach yielded estimated emission of 540 kg/h at the time-of-flight.

We compared our estimates for CH₄ emissions with a bottom-up estimate which is derived using the most recent 2016 U.S. Environmental Protection Agency inventory (38) and the 2015 oil and gas production activity data from DOGGR

(<http://www.conservation.ca.gov/dog/Pages/Index.aspx> (accessed June 2016). Following the methodology in Jeong et al. (2014), (39) we estimate an annual emission rate of 740 kg CH₄/h.

The overall uncertainty of the airborne estimate of CH₄ emission is affected by several independent factors. (9) We separately assessed the uncertainty due to interpolation errors (for CH₄ and wind vector components) using conditional simulations. (29) In our recent study we applied conditional simulations specifically to address the problems of atmospheric heterogeneity and provided details about its mathematical framework. (40) Briefly, conditional realizations (a.k.a. spatially consistent Monte Carlo simulations), represent equally probable realizations of a spatial random function. They are “conditioned” in the sense that each realization honors observed values at measurement locations. (29) Conditional simulations are affected by both the choice of theoretical covariance model and the parametrization of the model. We generated 500 conditional realizations of CH₄ and wind vector component fields (cross-covariances between them were not taken into account) and calculated resulting emissions for each combination of conditional realizations. The resulting variance in the emission estimate represents the interpolation uncertainty, and was found to be 112 kg/h (expressed as 1 σ), which represents ~21% of the determined emission value. Note that the emission probability distribution function resulting from the ensemble conditional realizations represents a range of possible solutions, rather than an actual error, and thus should not be directly compared to error reported in other studies, if they reflected actual error estimate.

In addition, we analyzed the sensitivity of the calculated fluxes to the wind vector measurement accuracy and tried to answer two questions: (a) what is the uncertainty of flux estimates given that the absolute accuracy of the horizontal wind vector calculated by MMS system was 0.1 m/s, and (b) what is the requirement for wind measurement accuracy in order to keep the emission uncertainty below 10% of the reported value. To address the first question, we simultaneously perturbed both U and V vector component by adding 0.1 m/s in the first run, and subtracting in the second, and calculated resulting emission estimates. The resulting error bounds were estimated to be -6.5 and +7.9 kg/h, respectively. To address the second question, we incrementally perturbed both V and U until the emission estimated departed from the initial value by 10%. The obtained results were -0.7

and +0.6 m/s (the average wind speed at all nodes of the grid was ~ 8.5 m/s). While the assumption of the wind stationarity is justified in cases of relatively short sampling times (~ 15 min in this study), a systematic change of the wind during the course of sampling would be manifested as a change with height, not with time, given that the aircraft typically samples vertically (for detailed domain size considerations see [SI](#)).

Apart from the analyzed sources of overall uncertainty, there are components of the uncertainty resulting from the absence of information about the eventual vertical mass transfer, inaccuracies in CH_4 measurement data, correlated transient wind vector and/or CH_4 measurement errors over the course of measurement, uncertainty resulting from the selection of theoretical covariance model and its actual parametrization (see Cambaliza et al., 2014, for a detailed overview).

3.4 Discussion

We modified four critical elements in the current urban outflow sampling protocols: flight pattern design, the way covariance is modeled to account for anisotropy, the selection of interpolation method that accounts for spatially variable mean (not implemented in this study following the variance-ratio test, but should remain a default approach in cases where clear vertical gradient is found or suspected), and the way mass balance is used to calculate the empirical correction factor for reducing wind measurement and interpolation errors.

The absolute flux variability through the grid was mainly driven by wind variability. Thus, the most intense fluxes are found near the top of the grid. However, useful information about source emission strength is contained within the lower portions of the grid, where absolute flux values through the grid are relatively small. This emphasizes the importance of accurate wind measurements and an accurate interpolation scheme for the mass-balance approach, as small errors in balancing the inflow and outflow of the air mass itself could yield substantial errors in flux estimates.

The method presented here bridges the gap between direct local flux quantification approaches, such as eddy covariance measurements, and methods that operate at larger spatial scales, based primarily on inverse modeling techniques. Its scalability depends purely on the size of the grid, availability of the observational data, and control of the basic prerequisites of the physics the approach is based upon.

Supporting Information

The Supporting Information is available free of charge on the [ACS Publications website](#) at DOI: [10.1021/acs.est.7b03100](https://doi.org/10.1021/acs.est.7b03100).

- The analysis of atmospheric anisotropy in the context of airborne measurements; considerations of the optimal domain size the proposed method is applicable to practical considerations, with an emphasis on reproducibility of the proposed method ([PDF](#))
- **PDF**
o [es7b03100_si_001.pdf \(325.83 kB\)](#)

Elliptic Cylinder Airborne Sampling and Geostatistical Mass Balance Approach for Quantifying Local Greenhouse Gas Emissions

1

S

upp

orting Information for:

Elliptic cylinder airborne sampling and geostatistical mass balance approach for quantifying local greenhouse gas emissions

Jovan M. Tadić

1,*

*

†

, Anna M. M

ichalak

1

, Lau

ra Iraci

2

, Velib

or Ilić

3

, Sébastien C. Biraud

4

, Daniel R.
Feldman

4

, Th

aopau

l Bui

2

, Matthew S. Johnson

2

, Max Loewenstein

2

, Seongeun Jeong

5

, Marc L.

Fischer

5

, Emma L. Y

ates

2

and

Ju-

Mee Ryoo

2

1

Department of Global Ecology, Carnegie Institution for Science, Stanford CA 94305 USA

2

Earth Science Division, NASA Ames Research Center, Moffett Field CA, USA

3

RT

-RK Institute for Computer Based Systems, 21000 Novi Sad, Serbia

4

Earth and Environmental Sciences Area, Lawrence Berkeley National Lab,

Berk

eley CA 94720 USA

5

Energy Technologies Area, Lawrence Berkeley National Lab,
Berkeley CA 94720, USA

†

Now at Earth and Environmental Sciences Area, Lawrence Berkeley National Lab, Berkeley CA 94720
USA

* C

Corresponding author at: Department of Climate Sciences, Lawrence Berkeley National Laboratory,
Berkeley CA 94720.

Correspondence to

: jotadic@lycos.com (J. M. Tadić)

, tel: ++1

-510-486-4865.

C

consisting of 3 Sections and 1 Figure within 4 pages.

2

The supporting information gives further details on the atmospheric anisotropy and kriging kernels
developed and used in this study to account for its presence.

Atmospheric anisotropy in the context of airborne measurements and flux quantification

Due to the variable and flexible shape of airborne trajectories,

airborne measurements can capture

properties of the atmospheric 3D fields in all directions providing information about two important

properties of the atmosphere: non-

stationarity (variable mean, variable covariance) and anisotropy

(zonally or directiona

lly

-dependent variability).

Anisotropy usually occurs in two forms, as (1) directional and (2) zonal anisotropy.

1- 4

Directional

(i.e., geometric) anisotropy, which can be reduced to the difference in decorrelation lengths in different

spatial directions, can be easily modeled by normalizing unit distance vectors along the principal axes of

anisotropy using decorrelations length values. Zonal (i.e., stratified) anisotropy represents a more serious

issu

e. Zonal anisotropy assumes differences in both decorrelation lengths and associated spatial variances

along different spatial directions, and occurs when the variogram is dependent on only some components

of the distance vectors (e.g. vertical distance).

1

A common approach to modeling zonal anisotropy

assumes creation of nested variogram structures for every subspace where zonal anisotropy occurs. Apart

from the problem of identification of principal axes (or subspaces) of anisotropy, modeling zonal

anisotropy represents a practical problem of simultaneous fitting of multiple parameters, which is a non

-

trivial task where the data are noisy.

Both types of anisotropy are pronounced in the atmospheric planetary boundary layer (PBL),

5- 7

representing a challenge to all interpolation techniques used in the studies of the atmospheric spatial

structure. In the absence of wind, the vertical pressure gradient and asymmetrical interfaces between

atmosphere and the rest of the Earth system breaks down the isotropic properties of the atmospheric

structure and divides it into horizontal and vertical subspaces. In the presence of wind the situation is

additionally complicated by subdivision of the horizontal subspace into two orthogonal components –

along and perpendicular to the wind vector. In our previous study

5

we analyzed a classical example of

[figshare](#)

Share [Download](#)

∇ Author Present Address

(J.M.T.) Earth and Environmental Sciences Area, Lawrence Berkeley National Lab, Berkeley
California 94720, United States.

The authors declare no competing financial interest.

-

Acknowledgment

This work was supported by the National Aeronautics and Space Administration through grant no. NNX08AJ92G, the National Science Foundation through grant no. 1342076, the California Energy Commissions Natural Gas Research program through grant no. 500-11-027, the Office of Biological and Environmental Research of the US Department of Energy under contract no. DE-AC02-05CH11231 as part of the Terrestrial Ecosystem Science and Atmospheric System Research Programs. AJAX measurements were supported through the NASA Science Innovation Fund and Ames Research Center Director's funds. All data used in this study are available upon request.

- [Reference QuickView](#)
-

References

This article references 40 other publications.

1. [1.](#)

The WHO Centre for Health Development, Kobe, and United Nations Human Settlements Programme (UN-HABITAT), Hidden cities: unmasking and overcoming health inequities in urban settings, accessible from <http://www.hiddencities.org/report.html>, **2010**.

2. [2.](#)

Committee on Methods for Estimating Greenhouse Gas Emissions. Verifying greenhouse gas emissions: method to support international climate agreements, *National Research Council*; National Academy Press:Washington, DC, **2010**.

3. [3.](#)

Hartmann, D. L.; Klein Tank, A. M. G.; Rusticucci, M.; Alexander, L. V.; Brönnimann, S.; Charabi, Y.; Dentener, F. J.; Dlugokencky, E. J.; Easterling, D. R.; Kaplan, A.; Soden, B. J.; Thorne, P. W.; Wild, M.; Zhai, P. M. Observations: Atmosphere and Surface. In *Climate Change: The Physical Science Basis. Contribution of Working Group I to the Fifth Assessment Report of the Intergovernmental Panel on Climate Change*; Stocker, T. F.; Qin, D.; Plattner, G.-K.; Tignor, M.; Allen, S.

K.; Boschung, J.; Nauels, A.; Xia, Y.; Bex, V.; Midgley, P. M., Eds.; Cambridge University Press: Cambridge, **2013**.

4. [4.](#)

McKain, K.; Wofsy, S. C.; Nehrkorn, T.; Eluszkiewicz, J.; Ehleringer, J. R.; Stephens, B. B. Assessment of ground-based atmospheric observations for verification of greenhouse gas emissions from an urban region. *Proc. Natl. Acad. Sci. U. S. A.* **2012**, vol. 109, (22) 8423– 8428. DOI: 10.1073/pnas.1116645109

[\[Crossref\]](#), [\[PubMed\]](#), [\[CAS\]](#)

5. [5.](#)

Yadav, V.; Michalak, A. M.; Ray, J.; Shiga, Y. P. A statistical approach for isolating fossil fuel emissions in atmospheric inverse problems *J. Geophys. Res. Atmos.* **2016**, 121, 12,490– 12,504 DOI: 10.1002/2016JD025642

[\[Crossref\]](#)

6. [6.](#)

Wunch, D.; Wennberg, P. O.; Toon, G. C.; Keppel-Aleks, G.; Yavin, Y. G. Emissions of greenhouse gases from a North American megacity. *Geophys. Res. Lett.* **2009**, 36, L15810, doi: DOI: 10.1029/2009GL039825, 2009.

[\[Crossref\]](#), [\[CAS\]](#)

7. [7.](#)

Mays, K. L.; Shepson, P. B.; Stirm, B. H.; Karion, A.; Sweeney, C.; Gurney, K. R. Aircraft-based measurements of the carbon footprint of Indianapolis *Environ. Sci. Technol.* **2009**, 43, 7816– 7823 DOI: 10.1021/es901326b

[\[ACS Full Text\]](#) , [\[CAS\]](#)

8. [8.](#)

Karion, A.; Sweeney, C.; Pétron, G.; Frost, G.; Hardesty, R. M.; Kofler, J.; Miller, B. R.; Newberger, T.; Wolter, S.; Banta, R.; Brewer, A.; Dlugokencky, E.; Lang, P.; Montzka, S. A.; Schnell, R.; Tans, P.; Trainer, M.; Zamora, R.; Conley, S. Methane emissions estimate from airborne measurements over a western United States natural gas field *Geophys. Res. Lett.* **2013**, 40 (16) 4393– 4397 DOI: 10.1002/grl.50811

[\[Crossref\]](#), [\[CAS\]](#)

9. [9.](#)

Cambaliza, M. O. L.; Shepson, P. B.; Caulton, D. R.; Stirm, B.; Samarov, D.; Gurney, K. R.; Turnbull, J.; Davis, K. J.; Possolo, A.; Karion, A.; Sweeney, C.; Moser, B.; Hendricks, A.; Lauvaux, T.; Mays, K.; Whet

stone, J.; Huang, J.; Razlivanov, I.; Miles, N. L.; Richardson, S. J. Assessment of uncertainties of an aircraft-based mass balance approach for quantifying urban greenhouse gas emissions *Atmos. Chem. Phys.* **2014**, 14, 9029– 9050 DOI: 10.5194/acp-14-9029-2014

[\[Crossref\]](#), [\[CAS\]](#)

10. [10.](#)

Karion, A.; Sweeney, C.; Kort, E. A.; Shepson, P. B.; Brewer, A.; Cambaliza, M. O. L.; Conley, S.; Davis, K. J.; Deng, A.; Hardesty, M. Aircraft-based estimate of total methane emissions from the Barnett Shale Region *Environ. Sci. Technol.* **2015**, 49, 8124 DOI: 10.1021/acs.est.5b00217

[\[ACS Full Text\]](#) , [\[CAS\]](#)

11. [11.](#)

Gordon, M.; Li, S.-M.; Staebler, R.; Darlington, A.; Hayden, K.; O'Brien, J.; Wolde, M. Determining air pollutant emission rates based on mass balance using airborne measurement data over the Alberta oil sands operations *Atmos. Meas. Tech.* **2015**, 8, 3745– 3765 DOI: 10.5194/amt-8-3745-2015

[\[Crossref\]](#), [\[CAS\]](#)

12. [12.](#)

Kort, E. A.; Frankenberg, C.; Miller, C. E.; Oda, T. Space-based observations of megacity carbon dioxide *Geophys. Res. Lett.* **2012**, 39, L17806 DOI: 10.1029/2012GL052738

[\[Crossref\]](#), [\[CAS\]](#)

13. [13.](#)

Virkkula, A.; Pohja, T.; Aalto, P. P.; Keronen, P.; Schobesberger, S.; Clements, C. B.; Petäjä, T.; Nikmo, J.; Kulmala, M. Airborne measurements of aerosols and carbon dioxide during a prescribed fire experiment at a boreal forest site *Boreal Environ. Res.* **2014**, 19153– 181

14. [14.](#)

Eliasson, J.; Yoshitani, J.; Weber, K.; Yasuda, N.; Iguchi, M.; Vogel, A. Airborne measurement in the ash plume from Mount Sakurajima: analysis of gravitational effects on dispersion and fallout *Int. J. Atmos. Sci.* **2014**, 2014, 1– 16 DOI: 10.1155/2014/372135

[\[Crossref\]](#)

15. [15.](#)

Conley, S.; Franco, G.; Faloon, I.; Blake, D. R.; Peischl, J.; Ryerson, T. B. Methane emissions from the 2015 Alison Canyon blowout in Los Angeles, CA *Science* **2016**, 351 (6279) 1317 DOI: 10.1126/science.aaf2348

[\[Crossref\]](#), [\[PubMed\]](#), [\[CAS\]](#)

16. [16.](#)

Pétron, G.; Karion, A.; Sweeney, C.; Miller, B. R.; Montzka, S. A.; Frost, G.; Trainer, M.; Tans, P.; Andrews, A.; Kofler, J.; Helmig, D.; Guenther, D.; Dlugokencky, E.; Lang, P.; Newberger, T.; Wolter, S.; Hall, B.; Novelli, P.; Brewer, A.; Conley, S.; Hardesty, M.; Banta, R.; White, A.; Noone, D.; Wolfe, D.; Schnell, R. A new look at methane and non-methane hydrocarbon emissions from oil and natural gas operations in the Colorado Denver-Julesburg Basin *J. Geophys. Res.: Atmos.* **2014**, 119 (11) 6836– 6852 DOI: 10.1002/2013JD021272

[\[Crossref\]](#), [\[CAS\]](#)

17. [17.](#)

Leen, J. B.; Yu, X.-Y.; Gupta, M.; Baer, D. S.; Hubbe, J. M.; Kluzek, C. D.; Tomlinson, J. M.; Hubbell, M. R. Fast in-situ airborne measurement of ammonia using a mid-infrared off-axis ICOS spectrometer. *Environ. Sci. Technol.* **2013**, 47, 10446– 10453, doi: DOI: 10.1021/es401134u , 2013.

[\[ACS Full Text\]](#) , [\[CAS\]](#)

18. [18.](#)

Peischl, J.; Ryerson, T. B.; Brioude, J.; Aikin, K. C.; Andrews, A. E.; Atlas, E.; Blake, D.; Daube, B. C.; de Gouw, J. A.; Dlugokencky, E.; Frost, G. J.; Gentner, D. R.; Gilman, J. B.; Goldstein, A. H.; Harley, R. A.; Holloway, J. S.; Kofler, J.; Kuster, W. C.; Lang, P. M.; Novelli, P. C.; Santoni, G. W.; Trainer, M.; Wofsy, S. C.; Parrish, D. D. Quantifying sources of methane using light alkanes in the Los Angeles basin, California *J. Geophys. Res.: Atmos.* **2013**, 118 (10) 4974– 4990 DOI: 10.1002/jgrd.50413

[\[Crossref\]](#), [\[CAS\]](#)

19. [19.](#)

Cambaliza, M. O. L.; Shepson, P. B.; Bogner, J.; Caulton, D. R.; Stirr, B.; Sweeney, C.; Montzka, S. A.; Gurney, K. R.; Spokas, K.; Salmon, O. E.; Lavoie, T. N.; Hendricks, A.; Mays, K.; Turnbull, J.; Miller, B. R.; Davis, K.; Karion, A.; Moser, B.; Miller, C.; Obermeyer, C. Whetstone, J.; Prasad, K.; Miles, N.; Richardson, S. Quantification and source apportionment of the methane emission flux from the city of Indianapolis *Elementa* **2014**, 3, 000037 DOI: 10.12952/journal.elementa.000037

[\[Crossref\]](#)

20. [20.](#)

Lavoie, T.; Shepson, P.; Cambaliza, M.; Karion, A.; Sweeney, C.; Kort, C.; Hirst, B.; Yacovitch, T.; Lan, X.; Lyon, D.; Alvarez, R.; Harriss, R. Measurements of Point Source Methane

Emissions in the Barnett Shale Basin *Environ. Sci. Technol.* **2015**, 49, 7904 DOI: 10.1021/acs.est.5b00410

[[ACS Full Text](#) ], [[CAS](#)]

21. [21.](#)

Department of conservation, 2015. 2015 Report of California oil and gas production statistics. Available at:ftp://ftp.consrv.ca.gov/pub/oil/annual_reports/2015/PR03_2015.pdf.

22. [22.](#)

Tanaka, T.; Yates, E.; Iraci, L. T.; Johnson, M. S.; Gore, W.; Tadić, J. M.; Loewenstein, M.; Kuze, A.; Frankenberg, C.; Butz, A.; Yoshida, Y. Two-Year Comparison of Airborne Measurements of CO₂ and CH₄ with GOSAT at Railroad Valley, Nevada. *IEEE Trans. Geosci. Remote Sens.* **2016**, 54 (8), doi: 4367 DOI: 10.1109/TGRS.2016.2539973 .

[[Crossref](#)]

23. [23.](#)

Hamill, P.; Iraci, L. T.; Yates, E.; Gore, W.; Bui, T. P.; Tanaka, T.; Loewenstein, M. A New Instrumented Airborne Platform for Atmospheric Research *Bull. Am. Meteorol. Soc.* **2016**, 97, 397– 404 DOI: 10.1175/BAMS-D-14-00241.1

[[Crossref](#)]

24. [24.](#)

Tadić, J. M.; Loewenstein, M.; Frankenberg, C.; Butz, A.; Roby, M.; Iraci, L. T.; Yates, E. L.; Gore, W.; Kuze, A. A comparison of in-situ aircraft measurements of carbon dioxide and methane to GOSAT data measured over Railroad Valley playa, Nevada, USA. *IEEE Trans. Geosci. Remote Sens.* **2014**, 52 (12), doi:7764 DOI: 10.1109/TGRS.2014.2318201 .

[[Crossref](#)]

25. [25.](#)

Li, J.; Heap, A. A review of spatial interpolation methods for environmental scientists. *Geoscience Australia*, Canberra, **2008**, 53, 137.

26. [26.](#)

Carlson, C. G.; Clay, D. E. The Earth Model – Calculating Field Size and Distances between Points using GPS Coordinates, Site-Specific Management Guidelines series-11, Potash & Phosphate Institute (PPI), **1999**.

27. [27.](#)

De Iaco, S.; Myers, D.; Posa, D. Space-time analysis using a general product–sum model *Stat. Probab. Lett.* **2001**, 52 (no. 1) 21– 28 DOI: 10.1016/S0167-7152(00)00200-5

[\[Crossref\]](#)

28. [28.](#)

De Cesare, L.; Myers, D. E.; Posa, D. Product– sum covariance for space– time modeling: an environmental application *Environmetrics* **2001a**, 12, 11– 23 DOI: 10.1002/1099-095X(200102)12:1<11::AID-ENV426>3.3.CO;2-G

[\[Crossref\]](#)

29. [29.](#)

De Cesare, L.; Myers, D.; Posa, D. Estimating and modeling space–time correlation structures *Stat. Prob. Lett.* **2001b**, 51 (no. 1) 9– 14 DOI: 10.1016/S0167-7152(00)00131-0

[\[Crossref\]](#)

30. [30.](#)

Chilès, J.-P.; Delfiner, P. *Geostatistics: Modeling Spatial Uncertainty*, 2nd ed.; John Wiley & Sons, Inc.:Hoboken, NJ, **2012**; doi: DOI: 10.1002/9781118136188.ch3 .

[\[Crossref\]](#)

31. [31.](#)

Tadić, J.; Ilić, V.; Biraud, S. Examination of geostatistical and machine-learning techniques as interpolators in anisotropic atmospheric environments. *Atmos. Environ.* **2015**, Vol 111, 28 DOI: 10.1016/j.atmosenv.2015.03.063 .

[\[Crossref\]](#), [\[CAS\]](#)

32. [32.](#)

Wackernagel, H. *Multivariate Geostatistics: An Introduction With Applications*, 2nd ed.; Springer: Berlin, **1998**.

[\[Crossref\]](#)

33. [33.](#)

Hengl, T.; Heuvelink, G.; Stein, A.; Comparison of kriging with external drift and regression kriging. Technical report 2003. International Institute for Geo-information Science and Earth 92 T. Hengl et al./Geoderma 120 (2004) 75–93 Observation (ITC) Enschede. http://www.itc.nl/library/Academic_output.

34. [34.](#)

Kitanidis, P. K. A variance-ratio test for supporting a variable mean in kriging *Math. Geol.* **1997**, 29 (3) 335–349 DOI: 10.1007/BF02769639

[\[Crossref\]](#)

35. [35.](#)

Gourdji, S. M.; Mueller, K. L.; Schaefer, K.; Michalak, A. M. Global monthly averaged CO₂ fluxes recovered using a geostatistical inverse modeling approach: 2. Results including auxiliary environmental data *J. Geophys. Res.* **2008**, 113, D21115 DOI: 10.1029/2007JD009733

[\[Crossref\]](#), [\[CAS\]](#)

36. [36.](#)

Trainer, M.; Ridley, B. A.; Buhr, M. P.; Kok, G.; Walega, J.; Hubler, G.; Parrish, D. D.; Fehsenfeld, F. C. Regional ozone and urban plumes in the southeastern United States: Birmingham, a case study *J. Geophys. Res.* **1995**, 100, 18823– 18834 DOI: 10.1029/95JD01641

[\[Crossref\]](#)

37. [37.](#)

Ekman, V. W. On the influence of the Earth's rotation on ocean currents *Arch. Math. Astron. Phys.* **1905**, 2, 1– 52

38. [38.](#)

U.S. EPA. Inventory of U.S. Greenhouse Gas Emissions and Sinks: 1990–2014. EPA 430-R-16-002, (2016) (<http://www.epa.gov/climatechange/ghgemissions/usinventoryreport.html> (accessed June 2016)).

39. [39.](#)

Jeong, S.; Millstein, D.; Fischer, M. L. Spatially explicit methane emissions from petroleum production and the natural gas system in California *Environ. Sci. Technol.* **2014**, 48, 5982– 5990 DOI: 10.1021/es4046692

[\[ACS Full Text\]](#) , [\[CAS\]](#)

40. [40.](#)

Tadić, J. M.; Michalak, A. M. On The Effect of Spatial Variability and Support on Validation of Remote Sensing Observations of CO₂ *Atmos. Environ.* **2016**, 132, 309 DOI: 10.1016/j.atmosenv.2016.03.014

[\[Crossref\]](#), [\[CAS\]](#)